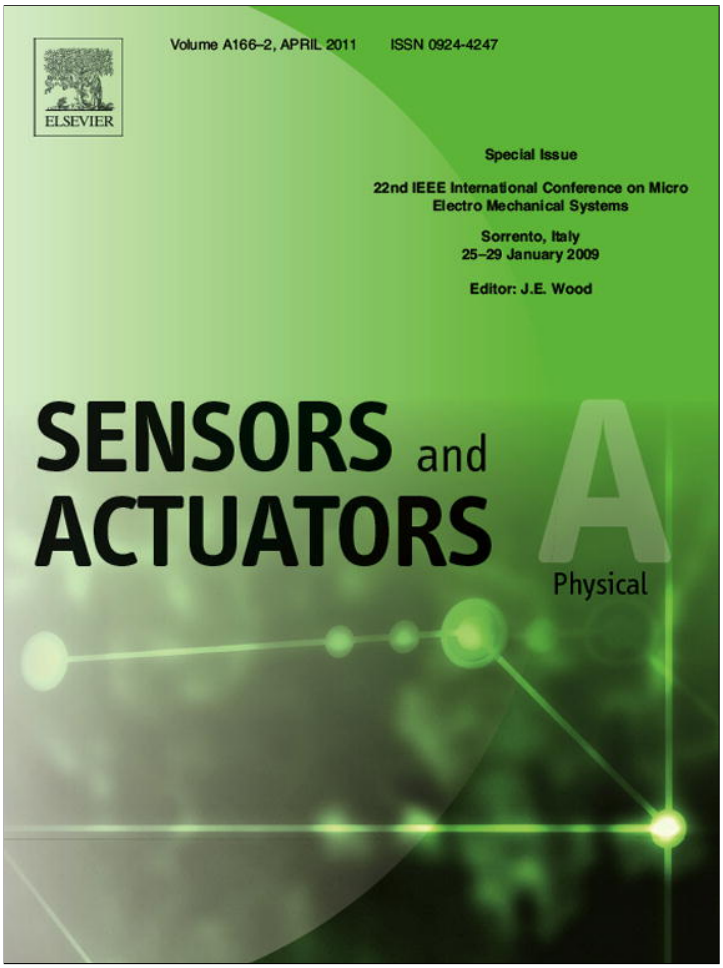

Sensors and Actuators A 166 (2011) 177–186

Contents lists available at ScienceDirect

Sensors and Actuators A: Physical

journal homepage: www.elsevier.com/locate/sna

Tensile measurement of single crystal gallium nitride nanowires on MEMS test stages

J.J. Brown[a,e,*], A.I. Baca[a,e], K.A. Bertness[b,e], D.A. Dikin[c,e], R.S. Ruoff[d,e], V.M. Bright[a,e]

[a] Department of Mechanical Engineering, University of Colorado - Boulder, Boulder, CO 80309-0427, USA
[b] Optoelectronics Division 815, National Institute of Standards and Technology, Boulder, CO 80305, USA
[c] Department of Mechanical Engineering, Northwestern University, Evanston, IL 60208, USA
[d] Department of Mechanical Engineering, University of Texas - Austin, Austin, TX 78712-0292, USA
[e] DARPA Center for Integrated Micro/Nano-Electromechanical Transducers (iMINT), University of Colorado - Boulder, Boulder, CO 80309-0427, USA

ARTICLE INFO

Article history:
Received 16 April 2009
Received in revised form 14 March 2010
Accepted 3 April 2010
Available online 18 April 2010

Keywords:
Tensile Loading
Gallium Nitride
Nanowire
Single Crystal
Mechanical Testing
MEMS

ABSTRACT

This paper reports direct tensile tests on n-type (Si-doped) gallium nitride single crystal nanowires[1] that were grown by nitrogen plasma-assisted molecular beam epitaxy and which are essentially free of defects and residual strain. Nanowires were integrated with actuated, active microelectromechanical (MEMS) devices using dielectrophoresis-driven self-assembly and platinum-carbon clamps created using a gallium focused ion beam. For one nanowire, failure strain of 0.042 ± 0.011 was found. Most nanowire specimens appeared to demonstrate tensile strength in the range of 4.0 ± 1.7 GPa to 7.5 ± 3.4 GPa. Failure modes included clamp failure, transverse (nanowire *c*-plane) fractures, and insufficient force from the MEMS test actuator.

1. Introduction

Gallium nitride is a direct wide-bandgap semiconductor with good thermal conductivity and notable optical, mechanical, piezoelectric, and transport properties. [1–4]. GaN nanowire cantilever resonators have been shown to have a high mechanical quality factor, which makes them appealing in nanomechanical devices. [1] Recent developments in the synthesis of gallium nitride nanowires have illustrated that these structures can be free of defects and residual strain. [5] These findings suggest that the nanowire morphology will offer numerous applications that would otherwise be unattainable in conventional epitaxial growth of this material. Integration of this material with active MEMS structures may allow development of new classes of tunable mechanical resonators, LEDs, lasers, and switches, among other possible new sensor and transducer technologies. Development of comprehensive mechanical data on gallium nitride nanowires (GaN NWs) will enable the realization of such new devices and applications. For instance, the ability to withstand 0.042 ± 0.011 tensile strain or 7.5 ± 3.4 GPa tensile stress, as reported here for one specimen, reflects exceptional strength and resilience for what might at first be considered a brittle material. This paper significantly expands upon the preliminary GaN tensile study given earlier [6].

The use of microfabricated structures enables mechanical testing of materials in small quantities or for which bulk sample preparation is difficult. Additionally, the integration of nanomaterial specimens on a MEMS mechanical tester serves as a test case for chip and wafer-scale integration of microtechnologies with a nanoscale material that has specific synthesis requirements. The data produced from these experiments are a step towards the thorough characterization of defect-free, single crystal GaN. There remain large sources of uncertainty associated with this mechanical system.

2. Experiment

2.1. MEMS test device

The MEMS mechanical test structure (Fig. 1) is a simplification of the one reported in references [7,8], consisting of a fixed stage electrically isolated from a moving stage that is laterally stabilized and actuated using a buckling beam thermal actuator. This test device

* Corresponding author at: Department of Mechanical Engineering, University of Colorado - Boulder, 427 UCB, Boulder, CO 80309-0427, USA.
E-mail address: Joseph.J.Brown@colorado.edu (J.J. Brown).
[1] Contribution of NIST, an agency of the U.S. government, not subject to copyright.

0924-4247/$ – see front matter © 2010 Elsevier B.V. All rights reserved.
doi:10.1016/j.sna.2010.04.002

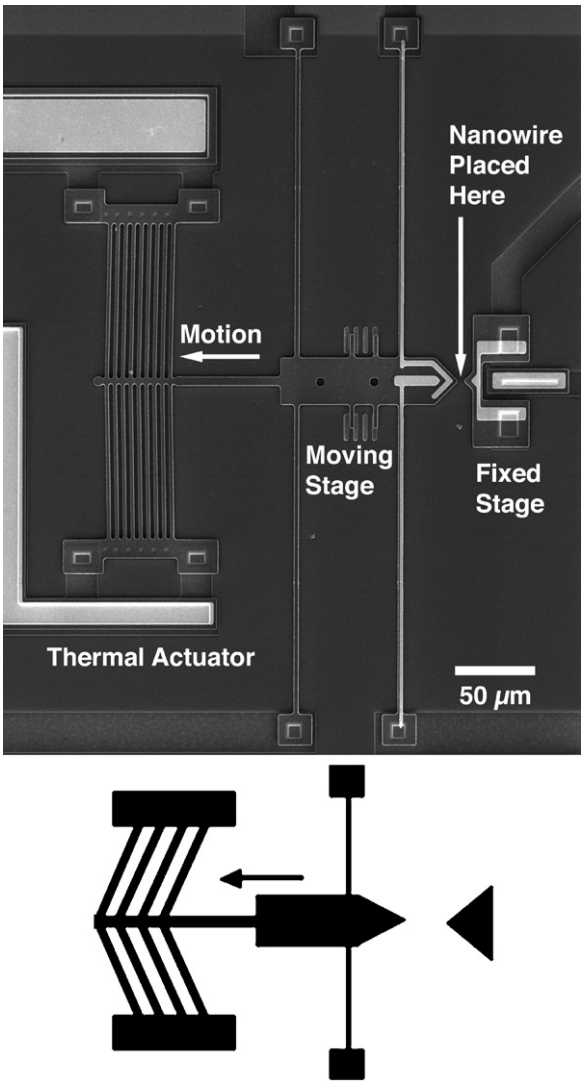

Fig. 1. (Top) Microfabricated tensile test structure consisting of electrically isolated moving and fixed stages. During a tensile test the moving stage moves away from the fixed stage. Thermal actuator beams are angled 89° from the direction of motion (reproduced from Ref. [6]). (Bottom) Simplified schematic of the device seen above (reproduced from Refs. [6,8]). The thermal actuator consists of an array of angled beams, which expand as current flows through them. The actuator pulls the moving stage, which is laterally stabilized by pairs of opposing beams.

was fabricated using the PolyMUMPS[2] surface micromachining service [9].

Stage motion is measured directly from scanning electron microscope (SEM) micrographs. The force applied by the stage can be computed using the approach described in Refs. [6–8], which is repeated here. The actual stage displacement d is compared to an expected displacement d_0. The force applied F is calculated according to Eq. (1) using the discrepancy between these displacements multiplied by the spring constant k of the system, which is calculated as discussed below.

$$F = k(d_0 - d) \tag{1}$$

During tensile tests, the MEMS test device was wirebonded to a 20-pin ceramic dual in-line package (DIP) chip carrier, and operated

[2] Mention of a specific product, service, or company does not constitute an endorsement by NIST. Other entities may provide similar or superior products or services.

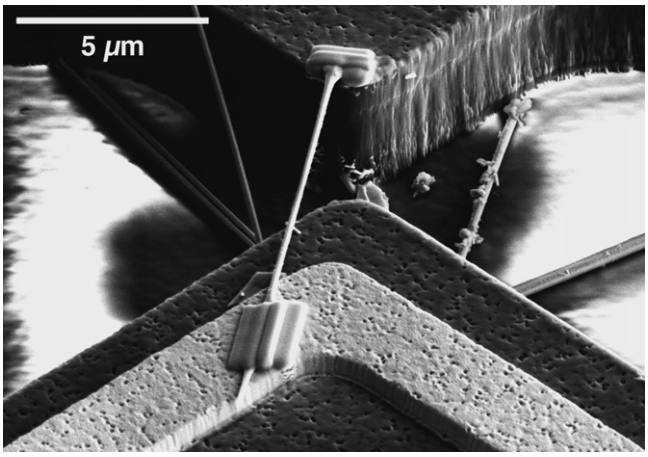

Fig. 2. The mounted GaN NW specimen #1, 200 ± 17 nm in diameter, was bonded to an unreleased tensile stage using Pt–C deposits formed using IBID (reproduced from Ref. [6]).

within a JEOL JSM-6480LV SEM. The test devices were connected to power electronics using an electrical feedthrough. Nanowire lengths were measured directly from SEM images. The equations used to map the nanowire length, stage displacement, and actuator power measurements into tensile curves of stress and strain are listed in Table 1.

In order to map experimental data onto force measurements using Eq. (1), a linear fit between free-moving displacement d_0 and input power P was used, $d_0 = BP$. The fit parameter B was calculated from a linear regression of d_0 and P data measured as output and input, respectively, of a freely moving test structure. Similar to prior work on other v-shaped thermal actuators, the d_0 vs. P curve as observed here for freely moving test systems is usually linear or slightly curved [10–12].

For a freely moving stage, displacement depends on thermal strain, which derives from temperature change and thermal expansion coefficients in the actuator beams. Due to the thermal resistance of the beams, the temperature profile of the beams depends upon the power dissipated within them, which can be measured by multiplying the current and voltage supplied to the actuator. Fitting to measured experimental curves allows the fit parameters to incorporate the nonuniform actuator temperature profile, the nonlinear thermal expansion and temperature-dependent changes in the electrical and thermal conductivities.

Table 1
Equations and variables used to derive tensile test measurements from data collected. The variables in boldface in the right hand column indicate values that were measured from experiments.

Equations	Variables
$\boldsymbol{\sigma = F/A}$	A = nanowire cross-section area
$\boldsymbol{A = \pi D^2/4}$	B = fitting parameter found with linear regression
$\boldsymbol{F = k(d_0 - d)}$	$\boldsymbol{D}$ = nanowire diameter
$\boldsymbol{d_0 = BP}$	$\boldsymbol{d}$ = actual displacement of tensile stage
$\boldsymbol{P = IV}$	d_0 = "expected" displacement of tensile stage
$\boldsymbol{e = L - L_0}$	e = nanowire elongation
$\boldsymbol{\varepsilon = e/L_0}$	ε = engineering strain
	F = force on nanowire
	$\boldsymbol{I}$ = current flow through actuator
	k = microsystem spring constant
	$\boldsymbol{L}$ = nanowire gauge length
	$\boldsymbol{L_0}$ = initial gauge length of the nanowire
	P = actuator input power
	σ = engineering stress
	$\boldsymbol{V}$ = voltage applied to actuator

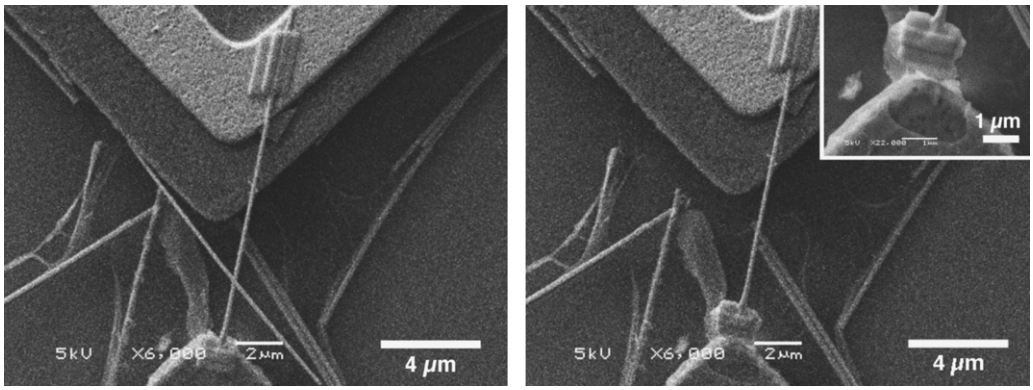

Fig. 3. Specimen 1, GaN nanowire under tensile load before (left) and after (right) failure of the bottom clamp (inset) at the interface between the clamp and the fixed stage. The area of the failed platinum/carbon clamp is approximately 3 μm^2. The additional nanowires and membrane-like material seen in these images are located underneath the suspended nanowire and MEMS test stage structures, and they were not in contact with the moving parts in this mechanical test (reproduced from Ref. [6]).

Many papers have reported investigations of v-type thermal actuators similar to the ones we have used here. [10–17] These investigations have shown relatively linear force vs. displacement behavior within several microns of the free-moving displacement.

Most attempts to calibrate the forces produced by a thermal actuator or other structures within a polycrystalline silicon device layer rely on the bending of a suspended beam formed from the same material and subjected to the same processing as the actuator. This approach relies on assumptions of Young's modulus E and dimensions of a beam in order to predict a spring constant k for that beam. [18] Some work has been done to verify k derived in this method with an alternate measurement derived from the resonance frequency of a suspended structure. [16] Better force measurement procedures are needed to verify the forces experienced by MEMS structures and this remains an active area of research.

The simulated behavior of systems that include v-type thermal actuators indicates that, as the power into the actuator increases, the force and displacement produced by the actuator also increase, but at rates that depend on the initial constraints of the actuator. [11,15] In Ref. [15] this manifests as the "load line" trajectory of a given microactuated system. In Refs. [11,15], it is seen in measurements that the simulation holds mostly true when $(d_0–d)$ is near 0, but at higher deviations from d_0 the force produced is significantly less than what is specified by simulation, due to a mode of beam buckling in the xy plane.

When temperature dependence of material properties used for simulation is neglected [8], simulation shows a clear linear relationship between F and d at a given input power, with $k = F_x/d$. This relation is easily related to predictions from beam mechanics as discussed below. For the force estimation discussed here, k is taken to be a constant value. This is the spring constant value valid for small perturbations of the spring and actuator system at $P = 0$, $d_0 = 0$, and $F_x = 0$. At higher input power levels, $\left|\frac{\partial F_x}{\partial d}\right|_{F_x=0}$ increases, indicating that Eq. (1) may systematically underestimate F. [11] Because high tensile strength and high elastic modulus are generally desirable, important properties, caution guides the observer to choose methods with systematic error such that, if it cannot be eliminated, it underestimates properties reported as the result of an experimental procedure. Due to the temperature dependencies in constitutive parameters, the assumption of beam bending with a constant k underestimates the actual force outputs, subject to the variation and accuracy of d, d_0, and k. In the absence of more traceable characterization of thermal actuators under varying input powers, displacements, and forces, the method used here provides a lower bound to forces and stresses derived from measurements taken with this MEMS system. Because the degree of the systematic underestimate is not known, this uncertainty is not included in the reported force, stress, and modulus values below.

2.2. Uncertainty

The uncertainties $u(xi)$ associated with the data presented here can be determined using similar mathematical analysis as that developed in Ref. [18], and following the guidelines described in Ref. [19]. Under this approach, uncertainties in measured data are evaluated statistically as the standard deviation of the mean of a data set (Type A evaluation) or according to a factor determined by an estimated probability distribution function for a given measurement (Type B evaluation). [19] For instance, where a bound of $\pm a$ is given on a measurement, the uncertainty u is evaluated from $u^2 = a^2/3$. [19] A combined standard uncertainty u_c for a measurement with multiple sources of uncertainty is found from the square root of the sum of the squares of the component uncertainties. In measurements that are derived from other data, as $y = f(x_i)$, the $u_c(y)$ can be found from the square root of the sum of the squares of the partial derivative of each x_i times each $u(x_i)$ [18,19].

For uncertainty values reported throughout this paper as $\pm nn$, this value nn represents the 95% confidence interval, which can be found by multiplication of the standard uncertainty $u(x_i)$ by a coverage factor of approximately 2. In Figs. 4–6, error bars show values of standard uncertainty $u(x_i)$ for each variable with no coverage factor included.

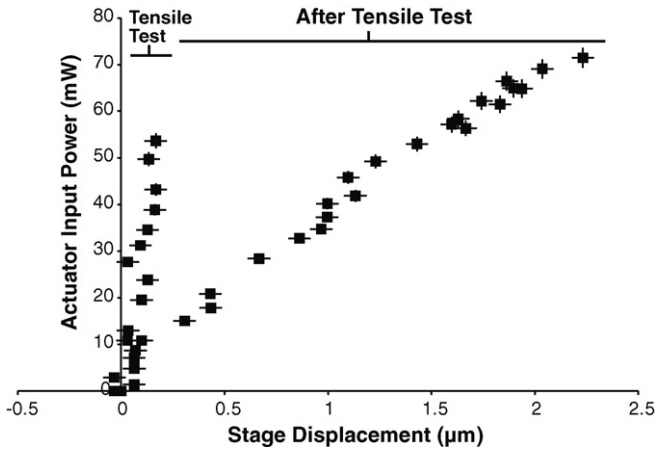

Fig. 4. Raw data from specimen 1 tensile test. Device input power and output displacement during the initial tensile test and then after the failure seen in Fig. 3.

Table 2
Measurements obtained to estimate u_c for beam widths.

Beam width (μm)	Combined standard uncertainty u_c (μm)	Number of measurements averaged	Image resolution (pixels/μm)	Comment
3.001	0.084	6	8	Unreleased
3.030	0.064	9	10	Released
2.93	0.13	8	4.75	Released

2.3. Test device spring constant

The maximum test system displacements d recorded here were about 3 μm and the minimum beam length was $L_B = 98.5$ μm. So, $d/L_B = 0.0304$. This is within the regime of small displacement approximation, so conventional solid mechanics beam deflection calculations for clamped beams can be used to approximate the spring constant k. In turn, k can be used to relate external force and displacement of a system of bending beams as represented by the test system in Fig. 1.

Significant sources of uncertainty in k include processing variations in beam dimensions and Young's modulus, and dependence of the spring constant on the given state of the actuator. This latter uncertainty is understood from the discussion above to be at a minimum for $P = 0$, $d_0 = 0$, and $F_x = 0$, and will not be included in the following uncertainty estimate.

Beam etch and width variation from batch to batch was measured from SEM images of one device seen before HF release and two devices after HF release (Table 2). For each device, the average and standard error were determined. The error due to pixel resolution in the source image proved to be more significant as a source of error than the uncertainty between measurement values, and therefore the uncertainty due to image resolution and was included with the standard error to give a combined standard uncertainty value.

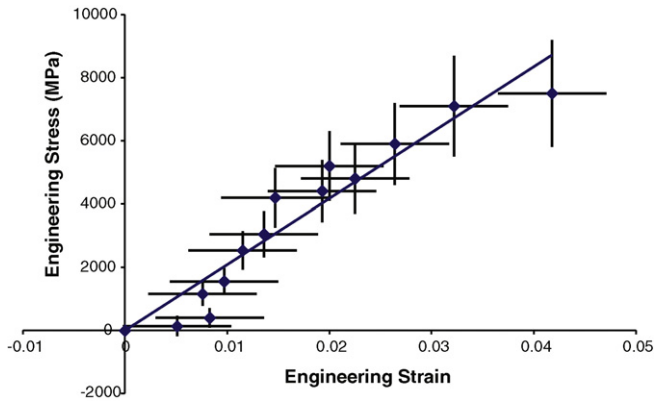

Fig. 5. Tensile test data for specimen 1. The regression line corresponds with a Young's modulus of 210 GPa. See the end of Section 4 for a discussion of the uncertainty of this value.

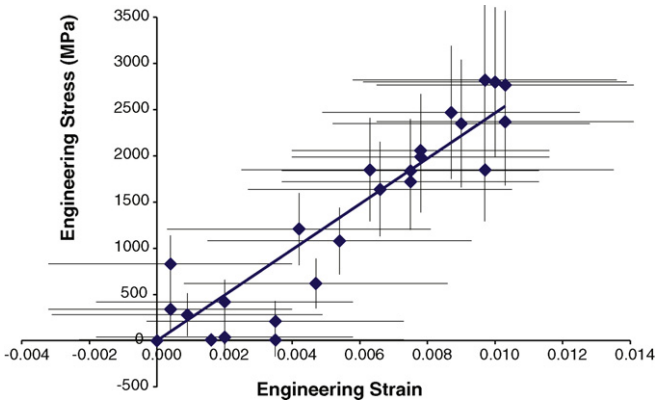

Fig. 6. Tensile test data for specimen 6, using σ computed according to Eq. (14). The regression line corresponds with a Young's modulus of 250 GPa. See the end of Section 4 for a discussion of the uncertainty of this value.

The maximum uncertainty in Table 2 was used as the value for in-plane dimensional uncertainty in the spring constant calculation. For the uncertainty due to thickness, a calculation based on manufacturing tolerance was used. The MEMS foundry specifies thickness of 3.50 μm with a tolerance of 0.25 μm. [20] Again using a Type B [19] evaluation, $u_c^2 = (0.25)^2/3$, so $u_c = 0.14$ μm. From 6 sets of measurements across 3 different chips and devices on a tilted SEM stage, a device thickness value of 3.36 μm with $u = 0.08$ μm was found. This measurement is within the foundry specification, but it does not include uncertainties due to tilt, so the foundry specification of 3.50 μm with $u = 0.14$ μm was used for the thickness in calculation of k. The in-plane Young's modulus of MUMPS polycrystalline silicon has been well characterized, and $E = 162 \pm 14$ GPa, determined from beams of similar dimension [21], was used as an input to the calculation of k. Assuming this value reported uncertainty according to standard practice of 95% confidence, the standard uncertainty is found by dividing by a coverage factor of 2, giving $u(E) = 7$ GPa [18].

By adding the individual spring constants computed according to the bending of each of the rectangular cross-section beams suspending the tensile test structure, it is readily verified that $k = 175$ μN/μm. The combined standard uncertainty for the spring constant of each component beam is then determined according to the root sum of squares of the individual uncertainties [18,19], and the total uncertainty in k was found by the arithmetic addition of each of these beam uncertainty values in order to give a maximum estimate of the uncertainty in k. This was found to be $u(k) = 29$ N/m.

Finite element simulations in CoventorWare software [22] corroborated the derived value of k. Additionally, we have used an atomic force microscope to do a preliminary measurement of k on a suspended structure with an identical array of beams and found an order of magnitude in the range specified here for k. (From the AFM measurement, $k = 150$ N/m with unknown $u(k)$.) Traceable measurement of k remains an ongoing aspect of work with MEMS test structures, but for the calculations below the calculated k and its corresponding $u(k)$ were used for derivation of force measurements.

2.4. Nanowire placement

Dielectrophoresis has been previously demonstrated [3,23] as a means of integrating nanowires to microfabricated structures in a wafer-level assembly technique. This method is less time-consuming than using micromanipulators to place individual nanowires. As seen in Figs. 2, 7 and 8, we have demonstrated that this self-assembly approach can be used to place nanowires on active MEMS devices.

The dielectrophoretic nanowire placement is performed using a modified probe station. Two electrical probes are placed in contact with electrical pads that allow an alternating (AC) electrical field to be applied across the fixed and moving stages. The stages

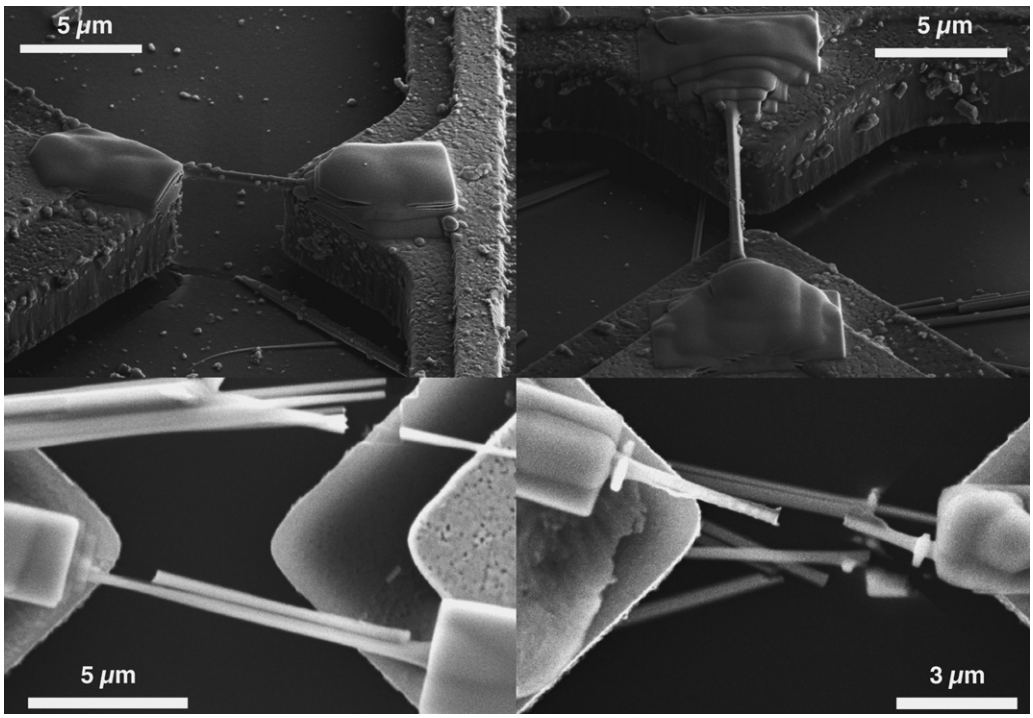

Fig. 7. (Upper left) Specimen 2. (Upper right) Specimen 3 as originally tested, after clamping and before an attempt to reduce the nanowire cross-section. (Lower left) Specimen 4. (Lower right) Specimen 5 just after failure.

taper to opposing points, where the nanowire placement is desired. Consequentially, there is a gradient in the amplitude of the electric field between these stages, with the maximum field at the location where the stages are closest. The nanowires polarize in the presence of an electric field, causing them to align parallel to the field lines. In the presence of the electric field gradient, nanowires are swept towards the field maximum, causing the nanowires to bridge the fixed and moving stages.

The *c*-axis oriented, Si-doped (n-type) GaN nanowires were synthesized by nitrogen plasma-assisted molecular beam epitaxy as described in Ref. [5]. A nanowire-liquid-suspension (roughly 2 mL in isopropanol) was formed by brief (2–5 min) sonication of a substrate supporting grown nanowires. The suspension was dispersed by a syringe that was positioned over the MEMS tester using a probe station micromanipulator. For the dielectrophoretic nanowire placement, a voltage of 10 V peak-to-peak amplitude was applied at 60–75 kHz to the opposing sides of the stage. While the electric field was applied, about 0.1 μL of the nanowire suspension was dispensed onto the stage. As the solvent evaporated, the surface tension of isopropanol and dielectrophoretic electrical forces caused the positioning of one or more nanowires across the gap between the moving and fixed stages. The dielectrophoresis parameters were derived through experimentation with voltage amplitude and frequency, and the values above were found to be most effective for the given stage and nanowires. This dielectrophoretic self-assembly process functions successfully for both unreleased and released MEMS structures. Solvent evaporation did not cause released MEMS structures to adhere to the fabrication substrate above which they were suspended.

2.5. Nanowire clamping

The nanowire specimens were clamped (Fig. 2) to the MEMS test structures using Pt–C deposits formed in a FEI NOVA 600i scanning electron beam and focused ion beam microscope (SEM-FIB) by ion beam induced deposition (IBID). This is similar to the approach taken in prior work. [24–26] For specimens 1–3, after deposition of the contacts, the test structure was released in aqueous HF and dried using supercritical CO_2. For specimens 4–6, the test structure was released and dried first, and then the nanowires and clamps were deposited onto the devices. GaN survives HF etching without significant damage. Occasionally the IBID Pt deposition process can

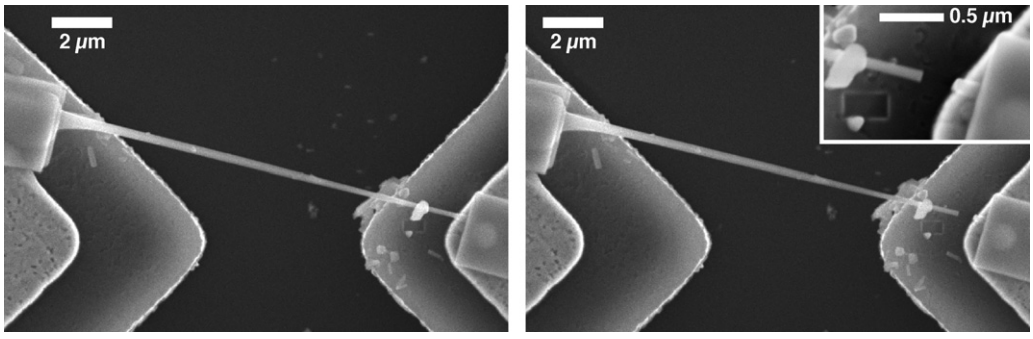

Fig. 8. (Left) Specimen 6 just before failure. Note the significant taper in this nanowire specimen. (Right) Specimen 6 just after failure. (Inset) Close-up view of the nanowire fracture, indicating a fracture mostly perpendicular to the long, *c*-axis of the nanowire.

leave extra platinum deposited on the nanowire specimen, as seen for specimen 2 in Fig. 7.

2.6. Measurements

Measurements of nanowire length and of stage motion were recorded from SEM images of the nanowire using ImageJ software. [27] Nanowire elongation e was computed directly from measurements of a specimen gauge length L defined between the clamps as observed in electron micrographs. Definition of the gauge length in this manner removes the effect of clamp deformation and specimen rotation from the recorded measurements of nanowire elongation and strain.

For specimens 1–3, current and voltage supplied to the MEMS actuator were measured using Hewlett-Packard 34401A multimeters or a Hewlett-Packard 3425A Universal Source. For specimens 4–6, the MEMS actuator was controlled by a National Instruments USB-6259 Data Acquisition System (DAQ) D/A converter feeding a signal to an op-amp current source circuit. The current passed through the actuator and a known resistor, and voltage follower circuits were used to read the voltage from nodes on each side of these loads. The voltage followers provided outputs to the A/D converter of the DAQ, which acquired and averaged 100 samples for each data point that was recorded. Current was measured from the voltage drop across the known resistor.

3. Analysis

Stress was calculated by dividing the force applied by the cross-sectional area of the nanowire. The cross-section area is found by measuring the nanowire diameter D from high-resolution images captured with the SEM capabilities of the FEI NOVA 600i dual beam microscope. For the calculations used in this paper, a circular cross-section of a diameter D has been assumed for all nanowire specimens. In reality, these are single crystals with imperfect hexagonal cross-sections. In the estimate of axial stress σ, a perfect hexagon of edge length $D/2$ can be inscribed into a circle of diameter D. The area of the hexagon is 17.3% less than the area of the circle. Alternately, a circle of diameter D can inscribe a hexagon with edge length $D\sqrt{3}/3$, underestimating the hexagon area by about 10%. The larger systematic uncertainty, 17.3% of a measured area, was treated as boundary, so $u^2(geometry) = (0.173A)^2/3$. This was included in the combined uncertainty for area measurements derived from nanowire diameter measurements.

3.1. Misalignment

In order to consider the motion and forces present within the nanowire specimen when it is not perfectly aligned with the axis of stage motion, it is helpful to set up multiple coordinate systems. Motion coincident with the motion of the tensile stage can be set in the Cartesian (x, y) system, with the nanowire end on the moving stage undergoing displacement δx. For misalignment analysis, an additional coordinate system may be specified coincident with the axis of the undeformed nanowire. For two-dimensional misalignment, this is a rotated Cartesian system (x', y') with the $\hat{x}'$ direction coincident with the nanowire and the $\hat{y}'$ direction perpendicular to the nanowire. In three dimensions a cylindrical coordinate system (x'', φ'', r'') is chosen, with the $\hat{x}''$ direction coincident with the nanowire and the $\hat{r}''$ direction perpendicular to the nanowire. The misalignment angle between the nanowire axis and the stage motion direction $\hat{x}$ is defined as θ.

In two dimensions, the end of the nanowire specimen on the moving stage experiences motion δx in the $\hat{x}$ direction. This may be transformed to motion in the (x', y') coordinate system according to $\delta x' = \delta x \cos\theta$ and $\delta y' = \delta x \sin\theta$.

In the case of three-dimensional misalignment, the out-of-plane misalignment distance ΔZ must also be considered with a small modification to θ. For a specimen with actual gauge length L_{actual} and misalignment angle γ in the xy plane, there is an out-of-plane angle β such that $\beta = \sin^{-1}(\Delta Z/L_{actual}) = \tan^{-1}(\Delta Z/L_0)$, if L_0 is measured as only a distance in the xy plane. The transformation of a vector in (x, y) into the three-dimensional nanowire coordinate system can by found by two successive Cartesian rotations (first about $\hat{z}$, then about $\hat{y}'$) followed by conversion from Cartesian to cylindrical coordinates (x'', θ'', r''). This gives misalignment angle θ as specified by Eq. (2). The extensional displacement $\delta x''$ and the perpendicular displacement $\delta r''$ of the nanowire end are specified by Eqs. (3) and (4), respectively. For typical values such as $\Delta Z = 500$ nm (approximately the case when one end of the nanowire rests on the silicon stage, and the other end rests on a metal pad on the silicon stage) and $L_0 = 10\,\mu$m, $\beta = 2.86^\circ$. The value $\cos\beta = 0.9988$, which is less than 0.2% modification to most calculations, so the effect of three-dimensional misalignment is not included in the uncertainty analysis below.

$$\theta = \cos^{-1}(\cos\gamma\,\cos\beta) \tag{2}$$

$$\delta x'' = \delta x \cos\theta = \delta x \cos\gamma \cos\beta \tag{3}$$

$$\delta r'' = \delta x \sin\theta \tag{4}$$

3.2. Clamp deformation

If there is no deformation within the clamp, the motion δx is identical to the stage displacement: $\delta x = d$. Because all forces opposing the motion of the MEMS test system are transmitted through the tensile specimen, they can be determined without the need to examine the complex stress state within the clamp in great detail. Strain is measured from nanowire gauge lengths specified between the end clamps on each nanowire specimen, therefore strain within the clamps does not contribute to the uncertainty of the strains recorded for the nanowire specimens.

3.3. Tensile forces in misaligned specimens

Stress values in the nanowires are estimated in Table 3 assuming fully uniaxial loading of the nanowires. The misalignment of the nanowires in several of the tensile tests creates the likelihood that that the actual stresses in the nanowires are somewhat larger than those estimated in Table 3. If the ends are treated as pinned rather than clamped, allowing the stress nonuniformities created by the bending moments at the clamps to be ignored, a free body diagram can be used to estimate the tensile force F_T in each nanowire. The tensile stage force F_x is calculated as discussed above, using Eq. (1). The sum of forces in the $\hat{x}$ direction equals zero: $F_x - F_T\cos\theta = 0$, rewritten as Eq. (5). The difference between F_T and F_x was computed and included in the uncertainty for the stress values in Table 3, but not in the reported stress values. Even for a 20° misalignment, only a 6% discrepancy is found, which is much less than the uncertainties that propagate from $u(k)$, $u(A)$, and $u(L)$ due to distance measurement uncertainty.

$$F_T = \frac{F_x}{\cos\theta} \tag{5}$$

3.4. Rotation

When bending is ignored, there is some rotation of the nanowire specimen due to displacement of the nanowire end. If the nanowire initial length is L_0 and the nanowire is displaced a distance δx in the direction of tensile stage motion $\hat{x}$, the nanowire stretches to final gauge length L and rotates an angle α (Eq. (6)). If rotation of the specimen is included in the analysis, Eq. (5) becomes Eq. (7). Eq.

Table 3
Tensile test data for six GaN nanowire specimens. A discussion of Young's modulus uncertainty values is located at the end of Section 4.

Specimen	Maximum engineering strain	Maximum engineering stress	Young's modulus E	Failure mode
1	0.042 ± 0.011	7.5 ± 3.4 GPa	210 GPa	Clamp Failure
2	0.031 ± 0.018	2.1 ± 0.6 GPa		*c*-plane fracture
3	0.022 ± 0.012			Insufficient force
4	0.0123 ± 0.0076	4.0 ± 1.7 GPa		Insufficient force
5	0.01 ± 0.01	4.7 ± 2.2 GPa		*c*-plane fracture
6	0.0103 ± 0.0036	7.1 ± 4.0 GPa	250 GPa	*c*-plane fracture

(7) is maximized when $\varepsilon = 0$ and θ is maximized. In this case, Eq. (7) reduces back to Eq. (5) and rotation does not contribute to the force uncertainty. For specimens 1 and 6, $\varepsilon > 0$ and $\theta > 0$, so Eq. (7) can be used to compute a value different from Eq. (5). For both specimens 1 and 6, the difference between F_T from Eq. (7) and F_T from Eq. (5) is only about 0.1%, so rotation due to elongation was not included in the uncertainty analysis for the data presented in Tables 3 and 4.

$$\alpha = \theta - \sin^{-1}\left(\frac{L_0 \sin\theta}{L}\right) = \theta - \sin^{-1}\left(\frac{\sin\theta}{1+\varepsilon}\right) \tag{6}$$

$$F_T = \frac{F_x}{\cos\left(\theta - \alpha\right)} = \frac{F_x}{\sqrt{1 - \frac{\sin^2\theta}{(1+\varepsilon)^2}}} \tag{7}$$

3.5. Bending

The nanowire ends are clamped and if it is assumed there is no deformation within the clamps, the nanowire is not subject to rotation. In this case, bending must be assumed to account for all motion that is not elongation of the nanowire. For a first analysis, motion in the $\hat{y}'$ direction is taken as pure bending, and motion in the $\hat{x}'$ direction is taken as pure elongation. The nanowire is assumed to be isotropic and have a constant circular cross-section along its length. The bending motion results from a force F_B in the $\hat{y}'$ direction that has a component in the original $\hat{x}$ direction, opposing the stage motion. Because the sum of forces in the $\hat{x}$ direction equals zero, $F_x = F_T \cos\theta + F_B \sin\theta$. Motion $\delta x'$ results from F_T (Eq. (8)) and bending can be described (Eq. (9)) by the beam equation for a slender beam with one end clamped and one end guided (free to displace but not to rotate), with applied force F_B, displacement $\delta y'$, and bending moment of inertia for a circular cross-section $I_0 = \pi D^4/64$.

$$\delta x' = \frac{F_T L_0}{AE} \tag{8}$$

$$\delta y' = \frac{F_B L_0^3}{12 E I_0} = \frac{16 F_B L_0^3}{3\pi E D^4} \tag{9}$$

$$\frac{\Delta F_T}{F_T} = \frac{3D^2 \tan^2\theta}{4L_0^2} \tag{10}$$

The systematic error in the tensile force due to the presence of the bending force can be examined using Eq. (10). For $L_0 = 10\,\mu$m NW, $D = 200$ nm, and $\theta = 10^\circ$, Eq. (10) yields $\Delta F_T/F_T = 10^{-5}$. Force error due to bending is a very minor effect and is therefore not included in uncertainty calculations.

If maximum stress within the nanowire is considered, this occurs where the maximum bending stress is added to tensile stress. The bending moment M within the nanowire is given by Eq. (11). The maximum bending stress $\sigma_{x',B}$ is at $(x', y') = (0, -D/2)$ or $(L_0, D/2)$. Axial bending stress is given by Eq. (12).

$$M = \tfrac{1}{2} F_B L_0 - F_B x' \tag{11}$$

$$\sigma_{x',B} = \frac{-Ey'}{EI_0 M} = \frac{-y'M}{I_0} \tag{12}$$

Using Eqs. (11) and (12), and relating the bending stress at the locations of maximum stress to the tensile stress due to elongation, $\sigma_{x',T}$, the maximum bending stress can be found:

$$Max.\sigma_{x',B} = \frac{3D\sigma_{x',T}\tan\theta}{L_0} \tag{13}$$

For the example values above, this means that $\sigma_{x',B}/\sigma_{x',T} = \sim 0.01$. In other words, bending stress nonuniformity can add about 1% error to the estimated tensile stress. This was not a significant contribution in comparison to the uncertainties due to force and area, so it was omitted from the calculation of combined stress uncertainty.

3.6. Strain uncertainty due to misalignment

Measurement of fiber length is repeated for each data point, with gauge length defined between the clamped regions. Therefore, uncertainty from in-plane rotation is not present in the elongation measurement used to derive the strain. Out-of-plane rotation of the nanowire specimen may lead to an overestimate of the actual strain. This can be evaluated following an approach similar to Eq. (7) or methods published for AFM tensile test misalignments [28,29]. For the typical $\beta = 2.86^\circ$ found earlier, and with a very large in-plane strain of $\varepsilon = 0.1$, this strain can be found to overestimate the actual strain by 0.3%, which is negligible in comparison to the other uncertainties in the strain. Uncertainty due to out-of-plane misalignment is therefore is not included in $u(e)$ and $u(\varepsilon)$.

Bending of the nanowire due to the clamped ends may have distorted the elongation measurement, which was performed using straight lines drawn on SEM images. The $u(\varepsilon)$ related to the bending is estimated as follows. A displacement δx of one end of a nanowire misaligned θ° will lead to a measured elongation $e_m = L - L_0$. The actual elongation e_a and hypotenuse δx, with angle θ and between

Table 4
Additional data for the six nanowire specimens. Angle of misalignment from stage motion direction, nanowire diameter D, linear fit parameter B, nanowire tensile test gauge length L_0, maximum power P reached during tensile test before observable damage to the MEMS actuator.

Specimen	Misalignment angle θ	D (nm)	B (μm/mW)	L_0 (μm)	Max. P (mW)
1	9.2 ± 0.4	200 ± 17	0.0280 ± 0.0011	10.13 ± 0.08	72 ± 4
2	11.6 ± 1.4	450 ± 20	0.0267 ± 0.0013	4.58 ± 0.06	96 ± 6
3	1.4 ± 1.0	±34	0.0267 ± 0.0013	9.29 ± 0.08	81 ± 4
4	14.1 ± 0.8	380 ± 20	0.02066 ± 0.00034	10.85 ± 0.06	134 ± 14
5	19.2 ± 1.4	344 ± 30	0.02066 ± 0.00034	5.85 ± 0.04	155 ± 16
6	13.56 ± 0.19	Min. 151 ± 30 Max. 380 ± 30	0.0264 ± 0.0011	13.97 ± 0.08	62.746 ± 0.038

sides e_a and δx define a right triangle that is inscribed within a circular sector of radius $L_0 + e_m$. Using this geometry, e_m can be related to the actual elongation e_a in the presence of bending according to Eq. (14). When divided by L_0^2, a relationship (Eq. (15)) between measured and actual strains, ε_m and ε_a, is derived.

$$e_a^2 \tan^2\theta = (e_m + L_0)^2 - (e_a + L_0)^2 \quad (14)$$

$$\varepsilon_a^2 \tan^2\theta = (1 + \varepsilon_m)^2 - (1 + \varepsilon_a)^2 \quad (15)$$

For $\theta = 10^\circ$ and $\varepsilon_a = 0.1$, the value $\varepsilon_m = 0.10014$ is found. Therefore, ε_m overestimates ε_a by 0.14%, and bending error in strain measurements can be omitted from the uncertainty calculation. Out-of-plane bending does not significantly modify this calculation.

There is additional localized strain variation from bending due to internal stress σ_x variations: $\pm\varepsilon_x = \sigma_x/E$, and this tends to add a similar percentage of uncertainty as the bending stress calculated in Eq. (13) contributes to the stress uncertainty. For example, for specimen 1, bending variations contribute $u(\varepsilon) = \sim 1.1\%$. Because measurement resolution uncertainties are about an order of magnitude larger or more, this localized bending uncertainty was not included in $u(\varepsilon)$.

4. Results

Tensile tests were performed on several nanowire specimens. These results are summarized in Tables 3 and 4, including the results of three tensile tests, specimens 4–6, performed after the initial results reported elsewhere [6]. From Table 3 it should be noted that the nanowire specimens are capable of withstanding significant strain.

Specimen 1 stands out in both the measured result and the accuracy of its strain measurement because its relatively long 10.13 ± 0.08 μm length and narrow 200 ± 17 nm diameter enabled it to stretch significantly under the load provided by the microfabricated test system. The tensile stress applied to the nanowire when the clamp failed was 7.5 ± 3.4 GPa.

The expected displacement d_0 used in force calibration for the specimen 1 test device was derived from motion of the stage after the specimen clamp failed (Fig. 4). This is a new development in tester calibration beyond the approach reported in Refs. [7,8], in that the fitting parameter between d_0 and P is derived from the same device which was used to perform a mechanical test. After specimen 4 and specimen 6 fractured, they were used to provide fitting parameters (in Table 4) for the test devices on which those specimens were mounted.

Specimen 2 did not appear to fracture during the tensile test, but subsequent high-resolution SEM examination and FIB cross-sectioning showed that the nanowire developed two fractures, one near each clamp.

FIB cross-sectioning also revealed that specimen 3 (Fig. 7) appeared to be two nanowires that had joined together during synthesis. This specimen had a large cross-sectional area of about 510 nm × 893 nm ($0.46\ \mu m^2 \pm 0.04\ \mu m^2$) and the force available from the actuator (about 340 ± 120 μN according to experimental data, giving a maximum tensile stress in this specimen of about 0.7 ± 0.3 GPa) was insufficient to cause failure of this structure in the tensile test reported in Tables 3 and 4. The FIB was used to reduce the cross-section of this specimen to about 250 nm × 290 nm. With a reduced cross-section, the specimen spontaneously buckled, likely due to damage or heating induced by FIB milling. When tensile stress was applied, failure occurred with more than 2.4 GPa stress applied to the resulting nanowire. This stress was estimated from the nanowire cross-section and the assumption of uniform loading. In reality, the specimen remained curved as it failed, indicating the presence of residual stress nonuniformity in the nanowire cross-section and a higher internal stress than is estimated with simple uniaxial tension.

The tensile tester MEMS device used to test specimen 4 was unable to provide sufficient force to induce failure of nanowire specimen 4 (Fig. 7). The MEMS actuator in the device used to test specimen 4 failed due to too much applied power. The nanowire specimen 4 did not fail during this tensile test. The maximum stress value reported in Table 1 reflects the highest value of force that was applied to this nanowire before the thermal actuator underwent observable plastic deformation.

Specimen 5 demonstrated very little elongation before it failed. It can be seen in Fig. 7 that the failure mode was another fracture perpendicular to the *c*-axis, although the edge of this fracture surface appeared to have been made irregular by some excess deposited platinum.

Elongation and failure were observed in specimen 6, Fig. 8. However, the presence of the taper of specimen 6 meant that the stress and strain were not uniform over the length of the nanowire. Although there was the same force transmitted over the length of the nanowire, the stress at the thick end was significantly less than the stress at the thin end. Assuming the elastic modulus was uniform throughout this specimen, the thin end experienced more stress and strain than the thick end. The nanowire failed at the thin end, indicating that an estimate of the maximum stress at failure (specimen 6, Table 3) should be found by dividing the force applied by the area at the thin end. The specimen 6 nanowire is obviously a tapered shape, which can be approximated as a conical prism with circular cross-section. Because elongation is measured for a gauge length that includes this significant taper, and this elongation value is used for computation of strain for this specimen, the calculation of stress used to compute Young's modulus E must also incorporate the effects of the taper. The elongation e relates to the tensile force F_T according to Eq. (16).

$$e = \frac{4F_T L_0}{\pi E D_1 D_2} \quad (16)$$

Here, D_1 and D_2 are the nanowire diameters at either end of L_0 and a circular cross-section is assumed. This elongation is equivalent to that of a uniform diameter cylinder with diameter $D_0 = \sqrt{D_1 D_2}$. For computation of E, the strain based on e/L_0 must be compared to a stress calculated using D_0, so a moderated stress σ (Fig. 8) is calculated from $\sigma = F_T/A = F_T/(\pi D_0^2/4) = F_T/(\pi D_1 D_2/4)$.

As seen in Table 3, $E = 210$ GPa was found for specimen 1 and $E = 250$ GPa was found for specimen 6. These are the slopes of the unweighted linear regression lines seen in Figs. 5 and 6, with the *y*-intercepts set to 0. The standard error of the regression for each of these values was $u = 10$ GPa, giving 95% confidence values of ±20 GPa. However, this value does not include the uncertainties of the stress and strain data points used to compute the regression line. When these values are added, the combined uncertainty of the derived modulus E could be as large as $u_c(E) = 60$ GPa for specimen 1 and $u_c(E) = 120$ GPa for specimen 6.

5. Discussion

The robust nature of specimen 1 in withstanding a 0.040 ± 0.017 engineering strain is perhaps the most notable result of this work. Image superposition confirms the strain measurement for this specimen. Observation of the specimen after the clamp failure indicates that it did not exhibit failure, nor did it experience plastic deformation. The estimated maximum stress applied to this nanowire, 7.5 ± 3.4 GPa appears to be a reasonable value in that the ultimate failure of specimens 3, 4, and 6 occurred for stress values of a similar order of magnitude.

The ability to withstand a large strain, as reported here for specimen 1, reflects an exceptional strain tolerance and resilience for

what might at first be considered a brittle material, but it is not entirely surprising given that this measurement was performed on a single crystal of a covalent material with a hexagonal lattice. These material characteristics are all known to increase mechanical strength. The lack of apparent extended and point defects in the nanowires also contributes to their strength.

Tensile strength and strain at tensile failure have not been widely reported for GaN, although there has been at least one report of compressive yield strength of 15 GPa in a GaN film. [30] Resonant frequency measurements on GaN NWs similar to those used here measured *c*-axis Young's modulus E_3 = 250–350 GPa. [1] Resonance experiments on other *a*-axis [120] oriented GaN NWs found E_1 = 227–305 GPa. [13] AFM 3-point bending on other *c*-axis GaN NWs found E_3 = 218–400 GPa, with a possible observation of diameter dependence of Young's modulus. [31] Elastic properties of GaN thin films and bulk crystals have been widely reported. Nanoindentation of epitaxially-grown GaN films with unspecified orientation found Young's modulus values in the range of 210–295 GPa. [30,32,33] Other types of experiments on bulk GaN crystals (ultrasonic, Brillouin scattering) have provided elastic constants C_{11}, C_{12}, C_{13}, C_{33} that can be used to find E_3, giving E_3 of 161 GPa (ultrasonic measurement) to 362 GPa (optical measurement) [34–37].

The modulus results mentioned above are in the correct range to fit with previously-reported values of the GaN E_3 but the uncertainties from this test system may be too large to make a definitive statement about values of E measured here. However, the maximum stress and strain values reported in Table 3 have 95% confidence intervals that are defined well enough to point to GaN NWs as resilient, high-strength materials.

Measurements from the JEOL SEM used to observe the tensile experiments are limited to the resolution of images obtained from this instrument. For the magnifications used for the data collected here, each pixel corresponds to about 20–30 nm. However, as noted in the 95% confidence values reported for the nanowire gauge lengths L_0 in Table 4, about ±40 nm is the best accuracy obtained from this instrument. Typical values were more on the order of ±80 nm in the measurements reported here due to the focal resolution of this SEM. Therefore, large displacements and large specimen gauge lengths will be more accurately recorded with SEM observation of MEMS testers than measurements of smaller distances. The nanowire gauge lengths are recorded in Table 4 to allow comparison of these measurements.

The failure shear stress of the specimen 1 clamp-microdevice interface was about 80 ± 30 MPa, which was much lower than might be expected for an interface with good bonding. After this failure occurred at the clamp-tester interface, potential sources of material that would interfere with good bonding between the clamp and the MEMS tester were noted.

It was observed that HF release after clamping nanowires to the microfabricated test stages using IBID can leave a membrane-like residue visible on the substrate of the test device (visible in Fig. 3). This residue can also form in instances where devices are subjected to SEM imaging followed by HF release, but it is not seen in cases where HF release is performed before imaging. This residue may originate from chemical decomposition of residual solvent adsorbed to the working surfaces, or of miscellaneous organic contamination from other molecules that were suspended in the solvent or present on other surfaces in the electron microscope. It appears to generate a resilient layer as a result of the SEM process. Alternatively, this may be errant Pt–C deposited as a byproduct of the IBID clamping procedure.

In applications where a good surface bond is desirable, such as the clamping of a nanomaterial specimen, FIB removal of potential bonding surface contamination is a quick and straightforward step, although some of the ablated material will nevertheless be redeposited. So, after the test on specimen 1 resulted in clamp failure rather than nanowire failure, the clamping procedure was modified. The gallium beam was used to remove an estimated 10 nm of material from the surface of the nanowire and the surrounding areas before clamp deposition. Furthermore, larger clamping areas of platinum were generated. Clamp failure was not observed in any subsequent tests.

The power at which the MEMS test structures begin to exhibit failure appeared to vary from chip to chip, likely dependent upon variations in processing of the chips holding these structures. For instance, devices used for earlier experiments reported in Ref. [6] displayed the onset of creep for input power the range of 60–90 mW. However, the device used to test specimen 4 withstood up to 134 ± 14 mW before it began to fail. This suggests that the fit parameter that correlates free displacement with input power is not a universal parameter but rather one that depends upon chip processing, most likely related to the HF release etch time. Therefore, at least one measurement of B must be made on each chip that is used for nanowire tensile testing. The four devices on each chip have identical structural configurations and identical processing histories, so the B value found with one device can be used for others on the chip.

The eventual thermal failure of the MEMS test structures manifests in several ways: the actuator resistance varies over time, SEM imagery shows discoloration in the vicinity of the hottest part of the actuator, and upon cessation of input power, the moving stage returns to a point closer to the fixed stage than when it began. These observations appear to indicate that the highest input powers also lead to plastic deformation of the thermal actuator.

6. Conclusion

This work has demonstrated that dielectrophoretic self-assembly of GaN nanowires can place nanowires on active MEMS devices without the need to separately manipulate individual nanowires. With careful design of suspended structures, this self-assembly process can operate on released structures without pulling these suspended structures into contact with the substrate. IBID platinum-carbon clamps can secure individual nanowires to a polysilicon surface for mechanical loading of the nanowires, but the interface between these clamps and the surface can fail with a shear stress on the order of 80 ± 30 MPa, therefore clamps must be deposited over a sufficient area to withstand the force applied to the nanowire specimen. Clamping is a key failure point and limiting fabrication step. Length measurements from SEM images are another significant limitation.

The MEMS test structures presented here have a moving stage that can be displaced by up to about 3 μm, but clamping of a tensile specimen across the moving and fixed stage creates a constraint which prevents motion of the moving stage, instead loading the tensile specimen. Measurement of specimen strain from SEM images removes the effect of clamp deformation from the tensile curve, but the clarity of tensile data was limited by image resolution. Measurements of electrical power are readily automated. Repeated tensile tests indicate that single crystal GaN appears capable of withstanding uniaxial strain at least 0.01 and as much as 0.040 ± 0.017. Furthermore, GaN NW tensile stress may reach the range of ~4–7 GPa without material failure.

Acknowledgements

This research was supported by are supported by the DARPA Center on Nanoscale Science and Technology for Integrated Micro/Nano-Electromechanical Transducers (iMINT Center) at the University of Colorado–Boulder, funded by the DARPA N/MEMS

S&T Fundamentals Program (HR0011-06-1-0048), Dr. D. L. Polla, Program Manager. J.J. Brown is supported by a National Science Foundation Graduate Research Fellowship. The authors thank Dr. Norman Sanford of NIST-Boulder, Boulder, CO, USA, for many helpful discussions, and Matthias Muoth and the ETH-Zürich Micro and Nanosystems group for help with AFM measurement. FIB machining and SEM imaging were performed at the Nanomaterials Characterization Facility of the University of Colorado at Boulder.

References

[1] S.M. Tanner, et al., High-Q GaN nanowire resonators and oscillators, Appl. Phys. Lett. 91 (2007) 203117.
[2] J.B. Schlager, et al., Steady-state and time-resolved photoluminescence from relaxed and strained GaN nanowires grown by catalyst-free molecular-beam epitaxy, J. Appl. Phys. 103 (2008) 124309.
[3] A. Motayed, et al., Realization of reliable GaN nanowire transistors utilizing dielectrophoretic alignment technique, J. Appl. Phys. 100 (2006) 114310.
[4] H.W. Seo, et al., Strained gallium nitride nanowires, J. Chem. Phys. 116 (2002) 9492–9499.
[5] K.A. Bertness, et al., Spontaneously grown GaN and AlGaN nanowires, J. Cryst. Growth 287 (2006) 522–527.
[6] J.J. Brown, et al., Tensile measurement of a single crystal gallium nitride nanowire, in: Tech. Digest IEEE MEMS 2009, Sorrento, Italy, January 25–29, 2009, pp. 642–645.
[7] J.J. Brown, et al., Microsystem for electromechanical measurements of carbon nanofiber loading and failure, in: Proc. Solid-State Sensors, Actuators, and Microsystems Workshop 2008, Hilton Head, SC, June 1–5, 2008, pp. 182–185.
[8] J.J. Brown, et al., Microsystem for nanofiber electromechanical measurements, Sens. Actuators A: Phys. 155 (2009) 1–7.
[9] MEMSCAP, Inc., Research Triangle Park, NC. http://www.memscap.com/en_mumps.html, 2009.
[10] M.J. Sinclair, A high force low area mems thermal actuator, in: 2000 Inter Society Conference on Thermal Phenomena, IEEE Press, 2000, pp. 127–132.
[11] M.S. Baker, et al., Final Report: Compliant Thermo-Mechanical MEMS Actuators, LDRD#52553, SAND2004-6635, Sandia National Laboratories, Albuquerque, NM, 2004.
[12] A.A. Geisberger, et al., Electrothermal properties and modeling of polysilicon microthermal actuators, J. MEMS 12 (2003) 513–523.
[13] D.L. Wilcox, L.L. Howell, Fully compliant tensural bistable micromechanisms (FTBM), J. MEMS 14 (2005) 1223–1235.
[14] Y. Zhu, et al., A thermal actuator for nanoscale *in situ* microscopy testing: design and characterization, J. Micromech. Microeng. 16 (2006) 242–253.
[15] J. Wittwer, M. Baker, L. Howell, Simulation, measurement, and asymmetric buckling of thermal microactuators, Sens. Actuators A: Phys. 128 (2006) 395–401.
[16] B. Peng, et al., A micromechanical system for nanoscale testing of one-dimensional nanostructures, Sens. Lett. 6 (2008) 1–12.
[17] T.L. Waterfall, et al., Simultaneous on-chip sensing and actuation using the thermomechanical in-plane microactuator, J. MEMS 17 (2008) 1204–1209.
[18] J.W. Wittwer, T. Gomm, L.L. Howell, Surface micromachined force gauges: uncertainty and reliability, J. Micromech. Microeng. 12 (2002) 13–20.
[19] International Organization for Standardization, Guide to the Expression of Uncertainty in Measurement, International Organization for Standardization, Geneva, Switzerland, 1993.
[20] J. Carter, et al., PolyMUMPS Design Handbook, Revision 11.0, MEMSCAP, Inc., Research Triangle Park, NC, 2005.
[21] W.N. Sharpe, et al., Tensile Testing of polysilicon, Exp. Mech. 39 (1999) 162–170.
[22] Coventor, Inc., Cary, NC. http://www.coventor.com, 2009.
[23] P.T. Blanchard, et al., MESFETS made from individual GaN nanowires, IEEE Trans. Nanotechnol. 7 (2008) 760–765.
[24] C.Y. Nam, et al., Disorder effects in focused-ion-beam-deposited Pt contacts on GaN nanowires, Nano Lett. 5 (2005) 2029–2033.
[25] C.Y. Nam, et al., Diameter-dependent electromechanical properties of GaN nanowires, Nano Lett. 6 (2006) 153–158.
[26] D. Tham, et al., Microstructure and composition of focused-ion-beam-deposited Pt contacts to GaN nanowires, Adv. Mater. 18 (2006) 290–294.
[27] ImageJ software, National Institutes of Health, Bethesda, MD. http://rsbweb.nih.gov/ij/, 2009.
[28] W. Ding, et al., Mechanics of crystalline boron nanowires, Compos. Sci. Technol. 66 (2006) 1112–1114.
[29] X. Li, et al., Effect of tensile offset angles on micro/nanoscale tensile testing, Rev. Sci. Inst. 76 (2005) 033904.
[30] R. Nowak, et al., Elastic and plastic properties of GaN determined by nano-indentation of bulk crystal, Appl. Phys. Lett. 75 (1999) 2070–2072.
[31] Y. Chen, et al., Mechanical elasticity of vapour–liquid–solid grown GaN nanowires, Nanotechnology 18 (2007) 135708.
[32] S.O. Kucheyev, et al., Nanoindentation of epitaxial GaN films, Appl. Phys. Lett. 77 (2000) 3373–3375.
[33] H.-Y. Huang, et al., Microbridge tests on gallium nitride thin films, J. Micromech. Microeng. 19 (2009) 095019.
[34] M. Yamaguchi, et al., Brillouin scattering study of gallium nitride: elastic stiffness constants, J. Phys.: Condens. Matter 9 (1997) 241–248.
[35] T. Deguchi, et al., Structural and vibrational properties of GaN, J. Appl. Phys. 86 (1999) 1860–1866.
[36] R.B. Schwartz, et al., Elastic moduli of gallium nitride, Appl. Phys. Lett. 70 (1997) 1122–1124.
[37] C.Q. Chen, et al., Size dependence of Young's modulus in ZnO nanowires, Phys. Rev. Lett. 96 (2006) 075505.

Biographies

Joseph J. Brown received an M.S. in Mechanical Engineering from the University of Colorado at Boulder in May 2008, and an A.B. in Engineering Sciences from Dartmouth College (Hanover, NH) in 2000. He is currently pursuing a Ph.D. in Mechanical Engineering at the University of Colorado at Boulder with interests in materials processing, and nanoscale characterization and patterning. He is co-author of 3 refereed journal articles and holds one patent.

Alicia I. Baca received her B.S. in Mechanical Engineering from the University of New Mexico (Albuquerque, NM) in the fall of 2007. At the University of Colorado, she is pursuing a Master's degree in Mechanical Engineering, focusing on the assembly of nanoscale materials into MEMS structures.

Kristine A. Bertness received in 1987 a Ph.D. in Physics from Stanford University, Stanford, CA. Prior to joining the National Institute of Standards and Technology (NIST) in 1995, she was at Varian Research Center and the National Renewable Energy Laboratory, Golden, CO. Her research focuses on semiconductor crystal growth, especially semiconductor nanostructures, and also optoelectronic device design and characterization. Recent work on wide-band-gap semiconductor nanowires earned her NIST team an R&D Micro/Nano 25 award. Bertness is a senior member of IEEE, has published roughly 100 papers, and has one patent.

Dmitriy A. Dikin received his Ph.D. degree from the Institute for Low Temperature Physics and Engineering at Kharkov, Ukraine in 1992. From 1992 to 1993, he was a Postdoctoral Fellow at Physics Institute, University of Würsburg, Germany. Currently, he is Research Professor at the Northwestern University, Evanston, IL. His research activities include study of physical and mechanical properties of nanotubes and nanowires, prototype NEMS device assembly, low noise electrical measurements, ultra-low and variable temperature measurements, electron microscopy and surface analysis. Dikin is a co-author of more than 60 refereed journal articles in the field of physics, mechanics, and material science.

Rodney S. Ruoff is a member of the faculty at the University of Texas at Austin, where he serves as a Cockrell Family Regents Chair in Mechanical Engineering. He received his B.S. in Chemistry from the U. of Texas (Austin) and Ph.D. from the University of Illinois-Urbana, in 1988. He was a Fulbright Fellow at the Max Planck Institute-Goettingen, Germany. His research activities include global environment and energy; synthesis and physical/chemical properties of nanostructures and composites; nanorobotics, NEMS, and new tools for biomedical research. Prof. Ruoff has published ~180 refereed journal articles.

Victor M. Bright received his BSEE degree from the University of Colorado at Denver, and the M.S. and Ph.D. degrees from the Georgia Institute of Technology, in 1989 and 1992, respectively. Dr. Bright is the Alvah and Harriet Hovlid Professor of Mechanical Engineering, Chair of the Mechanical Engineering Department, and the CEAS Faculty Director for Discovery Learning, at the University of Colorado at Boulder. From 2005 through 2007, he served as Associate Dean for Research, CEAS, CU-Boulder. During 2004 he was a Visiting Professor at ETH-Zürich, Switzerland. Prof. Bright's research activities include micro- and nano-electro-mechanical systems (MEMS and NEMS), silicon micromachining, microsensors/microactuators, opto-electronics, optical, magnetic and RF microsystems, atomic-layer deposited materials, MEMS reliability, and MEMS packaging. Prof. Bright is a Senior Member of IEEE, a Fellow of ASME, and an author of over 250 journal papers, conference proceedings, and book chapters. He is a Micromechanics Section Editor for the journal Sensors and Actuators A: Physical.